Diffusive homeostasis in a self-organizing recurrent neural network: Spatially dependent interaction as a determinant of neural activity and plasticity

Fabian Schubert[1🄮], Daniel Miner[1‡], Jochen Triesch[1†],

1 Frankfurt Institute for Advanced Studies, Frankfurt am Main, Germany

🄮This author performed parts of the programming, analysis and writing and contributed to the conceptualization.
‡This author performed parts of the programming, provided significant expertise and consultation and contributed to the conceptualization.
†This author provided significant expertise and consultation and contributed to the conceptualization.
* E-mail: fschubert@fias.uni-frankfurt.de

Abstract

The topology of cortical networks is subject to to constant change and the mechanisms involved in these dynamics are driven by the timing of neuronal spiking. Consequently, the success of a computational model of the self-organization of synaptic connectivity not only depends on the physiological accuracy of the plasticity mechanisms itself, but also on a realistic modeling of neuronal activity, e.g. since exact spike timing contains information on causal relations between pre- and postsynaptic activity. Experiments have found evidence for a strong heterogeneity among the average firing rates of cortical neurons, approximately following a log-normal distribution. In the context of synaptic plasticity it has been suggested that this property of neuronal firing has functional role in the formation of stable subnetworks. Furthermore, log-normal distributions are also known to well describe the statistics of synaptic efficacies in cortical networks.

We here present a self-organizing recurrent spiking network that exhibits log-normal statistics among the distribution of both synaptic weights, as well as of neuronal firing rates. To our knowledge, it is the first model that achieves this by means of a set of basic biologically motivated mechanisms, without the need for modifications that target specific experimental findings. Our model also comprises other features of synaptic connectivity that have been reported in experimental studies, such as an over representation of bidirectional connectivity.

The presented network model is a combination of a self-organizing spiking neural network (LIF-SORN) and a recently proposed mechanism known as diffusive homeostasis, which has been shown to allow for a heavy-tailed, log-normal distribution of firing rates. Further investigating this concept, we found that the spatial configuration of neurons could determine individual homeostatic targets of activity in our network model, raising the question whether this effect might play a role in real cortical networks.

Author summary

Using a combination of a self-organizing recurrent network model and a mechanism known as diffusive homeostasis, we could reproduce experimental findings on the

statistics of synaptic connectivities, as well as on the distribution of neuronal firing rates. It is the first recurrent network model to achieve this by means of a set of basic biological mechanisms, allowing the observed network structure and activity to develop autonomously without ad-hoc modifications targeting a particularly desired result. Moreover, by analyzing the diffusive control, we found that the statistics of firing rates within the network are strongly affected by fluctuations of neuronal spatial densities, which raised the question whether this effect could also be observed in real cortical networks.

Introduction

It has been shown experimentally that highly skewed, log-normal statistical distributions are present in cortical networks in the context of neuronal firing rates [1,2] as well as synaptic efficacies [3,4].

This heterogeneity of firing rates and synaptic efficacies is thought not to be involved in the preservation of stable synaptic structures while still allowing synaptic rewiring in order to adapt to changes in external stimuli [5,6]. Furthermore, a broad distribution of firing rates may serve to improve encoding of external stimuli [7]. Although the functional role of these statistical features have been investigated, the fundamental mechanisms required to give rise to these properties are still a point of debate. Combinations of additive STDP and multiplicative dynamics have been proposed as well as modified, weight dependent STDP rules in order to explain the heavy-tailed distribution of synaptic weights [8,9]. Furthermore, while synaptic efficacies do certainly affect neuronal activity, it is not clear whether a heavy-tailed distribution of weights is a necessary condition for the emergence of a correspondingly heavy-tailed distribution of neuronal firing rates, or if e.g. the intrinsic nonlinearity of the activation function of biological neurons is a sufficient explanation [10,11].

The interplay between synaptic connectivity and neuronal is further affected by homeostatic mechanisms that regulate neuronal firing rates on different timescales. Experimental studies have indicated that populations of neurons do not only exhibit broad distributions of firing rates, but also that these distributions are maintained on a single-cell level by means of individual homeostatic targets of activity [2,12]. However, the biological origin of these intercellular differences in target activity are still to be explored. Furthermore, homeostatic mechanisms should not interfere with transient, momentary changes, since it could potentially disturb information processing and transmission.

A model of diffusive homeostasis was introduced by Sweeney et al. [13], suggesting that diffusive signaling via nitric oxide (NO) could resolve this dichotomy between overall stability of firing activity and the need to allow a certain amount flexibility among individual neurons' activities. Through the diffusive signal, each neurons receives—intuitively speaking—a mixture of its own activity and its neighboring neurons. The overall population activity is thereby kept at a constant level, while allowing the overall distribution of firing rates to be approximately log-normal distributed.

We believe that a combination of diffusive homeostasis and the recurrent network model that has been investigated previously and referred to as LIF-SORN provides a realistic model of cortical activity and self-organization. This paper presents and discusses the results of this approach with respect to the aforementioned aspects: Developing a recurrent network structure that gives rise non-random statistical features found in experiments while at the same time exhibiting stable neuronal activity, resembling a log-normal distribution of firing rates. Furthermore, we predicted excitatory activity on the level of individual cells by an analytic approach, thereby gaining an understanding of the relation between spatial structure and firing rates. In

Table 1. Parameters of synaptic connections.

parameter	EE	EI	IE	II
connection fraction	$\rightarrow 0.1$	0.1	0.1	0.5
initial connection strength	$0.0001\,\mathrm{mV}$	$1.5\,\mathrm{mV}$	$-1.5\,\mathrm{mV}$	$-1.5\,\mathrm{mV}$
conduction delay	$1.5\,\mathrm{ms}$	$0.5\,\mathrm{ms}$	$1.0\,\mathrm{ms}$	$1.0\,\mathrm{ms}$

the face of possible new features within the network's structure, we clarify the causal   43
relation between diffusive spatial interaction and synaptic topology.   44

Materials and methods   45

Network simulation   46

400 excitatory LIF neurons and 80 inhibitory LIF neurons were assigned random   47
positions across a square area of $1000 \times 1000\,\mu\mathrm{m}$. All except recurrent excitatory   48
synapses were randomly generated before the start of the simulation until a desired   49
connection fraction was reached. The connection probability between two neurons was   50
calculated from a distant dependent Gaussian function with a standard deviation of   51
200µm. For excitatory to inhibitory (EI) and inhibitory to excitatory (IE) synapses, the   52
connection fraction was set to 0.1, and 0.5 for recurrent inhibitory synapses (II). These   53
connections were kept at a fixed connection strength throughout the simulation.   54
Furthermore, all synapses were simulated with a fixed (distance independent)   55
conduction delay. See Table 1 for a summary of parameters.   56
    Recurrent excitatory synapses were subject to a number of plasticity mechanisms to   57
be described in the following.   58

Synaptic plasticity   59

Synaptic Growth: New synapses are generated at an average rate of 920 per second.   60
For efficiency, this was implemented by drawing an integer number from a normal   61
distribution with mean 920 and standard deviation $\sqrt{920}$ once per second and   62
simultaneously inserting this number of synapses. This growth rate was tuned to   63
achieve the desired target concentration of 0.1 (see Table 1).   64
    Synaptic Pruning: The process of synaptic pruning was similarly carried out by   65
checking for EE synapses below a threshold of $10^{-6}\,\mathrm{mV}$ once each second (same instant   66
as growth) and removing them simultaneously, and thus adding them again to the set of   67
"potential" connections from which the growth process draws new connections.   68
    Spike Timing Dependent Plasticity: An additive STDP rule was used as
described e.g. in [14]. The change of weight between two neurons due to a pre- and
postsynaptic spike $(i \rightarrow j)$ is defined as:

$$\Delta w_{ji} = \sum_k \sum_l W(t_j^l - t_i^k) \tag{1}$$

$$W(\Delta t) = A_+ \exp(-\Delta t/\tau_+), \qquad \Delta t \geq 0 \tag{2}$$

$$W(\Delta t) = A_- \exp(\Delta t/\tau_-), \qquad \Delta t < 0 \tag{3}$$

Indexes k and l refer to the k-th and l-th pre- and postsynaptic spike respectively.   69
Parameters were chosen to approximate data from [15] and [16], namely $\tau_+ = 15\,\mathrm{ms}$,   70
$A_+ = 15\,\mathrm{mV}$, $\tau_- = 30\,\mathrm{ms}$ and $A_- = -7.5\,\mathrm{mV}$. However, we used the "nearest neighbor"   71
approximation for the sake of reduction of computational effort, only calculating the   72
effect of the most recent pre-post pair of spikes for potentiation and post-pre pair for   73

depression, yielding roughly the same value as the full summation due to the fast decay   74
times τ_+ and τ_- of the STDP-window.   75

Synaptic Normalization: For the same reasons of efficiency, synaptic   76
normalization was applied at the same rate as synaptic growth/pruning, updating each   77
w_{ji} from neuron i to neuron j as follows: 78

$$w_{ji} \to w_{ji} \frac{w_{\text{total}}}{\sum_i w_{ji}} \qquad (4)$$

w_{total} was set to different values for each of the four types of connections between the   79
excitatory and inhibitory pool of neurons. Except for the dynamically populated   80
EE-synapses these values could be directly set in accordance with the previously given   81
parameters of desired mean individual connection strength, size of the presynaptic   82
population and connection fraction, by calculating $w_{\text{total}} = w_{\text{mean}} N_{\text{presyn.}} p_{\text{conn.}}$, where   83
w_{mean} is given by the initial synaptic strength in Table 1, $N_{\text{presyn.}}$ is the number of   84
neurons and $p_{\text{conn.}}$ is the synaptic connection probability given in Table 1. This yielded   85
$w_{\text{total,EI}} = 60\,\text{mV}$, $w_{\text{total,IE}} = -12\,\text{mV}$, $w_{\text{total,II}} = -60\,\text{mV}$. $w_{\text{total,EE}}$ was set to $40\,\text{mV}$,   86
corresponding to a mean synaptic weight of $1\,\text{mV}$, given a targeted EE-connection   87
fraction of 0.1 and a population of 400 excitatory neurons.   88

Short Term Plasticity: A short term plasticity (STP) mechanism acting on   89
recurrent excitatory connections was implemented as presented in [17] as an additional   90
stabilization of network activity. It modulates the effective synaptic weights by   91
multiplying the value stored in the weight matrix w_{ji} by two dynamic variables x and u,   92
$w_{ji}^{\text{effective}} = w_{ji} \cdot x \cdot u$, each synapse owning a pair (x, u). The dynamics of these   93
variables are given by: 94

$$\dot{x} = \frac{1 - x}{\tau_d}, \; \dot{u} = \frac{U - u}{\tau_f} \qquad (5)$$

Each presynaptic spike furthermore causes a change of x and u by   95

$$x \to x - x \cdot u, \; u \to u + U(1 - u) \qquad (6)$$

We chose $U = 0.04$, $\tau_d = 0.5\,\text{s}$ and $\tau_f = 2\,\text{s}$ as a rough approximation of the values that   96
were experimentally observed [17]. For our choice of variables, a Poisson input with a   97
constant rate achieves the best synaptic transmission at a rate of $\sim 4.5\,\text{Hz}$,   98
corresponding to $x \cdot u \approx 0.2$. *Potentiation* in this context refers to the fact that stronger   99
input strengthens synaptic transmission compared to close to zero incoming spikes.   100

Neuron model   101

We used a leaky integrate-and-fire-model with a simple additive synaptic transmission   102
model for all neurons in the network, whose dynamics are described by a stochastic   103
differential equation: 104

$$\tau_m dV_i = -\left(V_i - E_l\right) dt + \sqrt{\tau_m} \sigma dW_i + \tau_m \sum_{j,k} w_{ij}^{\text{effective}} \delta\left(t_{\text{spike},j}^k + t_{\text{delay}} - t\right) \quad (7)$$

where V is the membrane potential, E_l is the equilibrium membrane potential, τ_m is the   105
membrane time constant, σ is the standard deviation of the noise term and dW is the   106
standard Wiener process. A neuron is generates a spike when its membrane potential   107
reaches the threshold voltage V_t. The voltage is then reset to V_r. A refractory period   108
was not implemented. A presynaptic spike causes a simple (delayed, see Table 1)   109
increment of the membrane potential of the postsynaptic neuron by $w_{ji}^{\text{effective}}$. Table 2   110
summarizes the aforementioned set of parameters.   111

Table 2. Parameters of LIF neuron.

parameter	exc. neur.	inh. neur.
E_l	-60 mV	-60 mV
τ_m	20 ms	20 ms
V_r	-70 mV	-60 mV
σ	$\sqrt{5}$ mV	$\sqrt{5}$ mV
V_t	subject to IP	-58 mV

Intrinsic plasticity

Apart from dynamic processes within synapses which contribute to a stabilization of the network's activity, neurons possess internal mechanisms capable of maintaining a desired regime of activity. Regular-spiking cells are known to down-(up-)regulate their firing rate upon increased (decreased) input on a timescale of tens of milliseconds [18, 19]. The network itself was not expected to exhibit fast changes of synaptic input since our simulation did not incorporate any rapidly changing external drive, which allowed us to neglect this feature. On the other hand, a similar form of adaption as a reaction on deprived or enhanced input can be observed on a timescale of hours to days [20]. In the latter case, a long-term change in excitability can be attributed to an altered number of permeable ionic channels. This contrasts the former short-term adaption, which can be explained by a separation of timescales among different ionic currents in the cell. A simple form of low intrinsic homeostasis was implemented in the original LIF-SORN by altering the neurons' firing threshold based on the deviation from a target firing rate. During the research reported by this paper, we implemented a new model of slow intrinsic homeostasis, based on the work presented in [13]. The following section describes both models in further detail.

Our original model of homeostatic control was described by the following differential equation:

$$\dot{V}_t = \eta_{\text{IP}}(r - r_{\text{IP}}) \tag{8}$$

with r as the neuron's firing rate and r_0 the target firing rate, η_{IP} the rate of threshold adaptation and r the estimated firing rate of a single excitatory neuron. In practice, this was implemented in discrete steps of $\Delta t = 0.1$ ms, estimating the firing rate by $r = N_{\text{spikes}}/\Delta t$, with N_{spikes} as the number of spikes within each interval.

The new diffusive homeostatic model by Sweeney et al. consists of a set of differential equations:

$$\dot{[\text{Ca}^{2+}]}_i(t) = -\frac{[\text{Ca}^{2+}]_i}{\tau_{\text{Ca}^{2+}}} + Ca^{2+}_{\text{spike}} \sum_j \delta(t - t_{\text{spike},i,j}) \tag{9}$$

$$\dot{[\text{nNOS}]}_i(t) = \frac{1}{\tau_{\text{nNOS}}} \left(\frac{[\text{Ca}^{2+}]_i^3}{[\text{Ca}^{2+}]_i^3 + 1} - [\text{nNOS}]_i \right) \tag{10}$$

$$\dot{[\text{NO}]}(\mathbf{r}, t) = -\lambda[\text{NO}] + D\nabla^2[\text{NO}] + \sum_i \delta^2(\mathbf{r} - \mathbf{r}_{\text{neur.},i})[\text{nNOS}]_i \tag{11}$$

$$\dot{V}_{t,i}(t) = \frac{[\text{NO}](\mathbf{r}_{\text{neur.},i}, t) - [\text{NO}]_0}{[\text{NO}]_0 \tau_{V_t}} \tag{12}$$

A depolarization within a nerve cell upon a spike-event t_{spike} causes a fixed inflow of ionic current Ca^{2+}_{spike}, which is modeled as an instantaneous increase of the $[\text{Ca}^{2+}]$ concentration. The concentration decays exponentially by a time constant $\tau_{\text{Ca}^{2+}}$. Though Ca^{2+} currents can be described in a much more detailed fashion, it can be considered as a reasonable approximation [21, p. 198-203]. The influence of $[\text{Ca}^{2+}]$ onto

Table 3. Parameters of homeostatic intrinsic plasticity.

parameter	value
r_{IP}	$3\,\mathrm{Hz}$
η_{IP}	$0.1\,\mathrm{mV}$
Ca^{2+}_{spike}	1
$\tau_{Ca^{2+}}$	$10\,\mathrm{ms}$
τ_{nNOS}	$100\,\mathrm{ms}$
D	default: $10\,\mu\mathrm{m}^2\mathrm{ms}^{-1}$
λ	$0.1\,\mathrm{s}^{-1}$
τ_{V_t}	$2500\,\mathrm{s}$

[nNOS] was modeled by Sweeney et al. through (10) using the Hill equation [22] to model a cooperative binding mechanism. The rate of [nNOS] is then fed into the "pool" of nitric oxide via point sources located at the neurons' positions. An additional decay term was added apart from the inflow and the diffusive term to provide a stable finite [NO] concentration under constant neuronal activity.

Finally, the dynamics of firing thresholds $V_{t,i}$ were modeled such that the rate of change is proportional to the relative deviation of NO concentration at the neurons' locations from a global target concentration $[NO]_0$.

To acquire a target concentration $[NO]_0$ corresponding to the desired mean firing rate, we let the system run with the previous homeostatic mechanism, still solving Eq. (9)-(11) until a steady mean over the concentrations at the neurons' positions was reached. This mean was then set to be the target concentration and we switched to diffusive homeostasis. Table 3 summarizes the choice of parameters that were introduced in this section. Diffusion parameters roughly match those measured in experiments [23].

Simulation of diffusion

We solved (11) with the finite difference method on a grid $\mathbf{r}_{i,j}$ with a resolution of 100×100 points. Integration over time was carried out by a 4th-order Runge-Kutta method with a time step of $1\,\mathrm{ms}$. $\nabla^2 NO(\mathbf{r}_{i,j}) = \nabla^2 NO_{i,j}$ was approximated by

$$\nabla^2 NO_{i,j} \approx \frac{NO_{i+1,j} + NO_{i-1,j} + NO_{i,j+1} + NO_{i,j-1} - 4NO_{i,j}}{h^2} \tag{13}$$

on each time step, where $h = L/100$ is the distance between neighboring grid points, determined by the length L of the square sheet and the resolution of the numeric grid. We implemented three possible boundary conditions:

1.) Periodic boundary conditions:

$$NO_{i,N_{\mathrm{grid}}} = NO_{i,0} \tag{14}$$

$$NO_{N_{\mathrm{grid}},i} = NO_{0,i} \tag{15}$$

$$NO_{i,-1} = NO_{i,N_{\mathrm{grid}}} \tag{16}$$

$$NO_{-1,i} = NO_{N_{\mathrm{grid}},i} \tag{17}$$

with N_{grid} being the grid resolution.

2.) Neumann boundary conditions with $\nabla NO = (0,0)$ at the boundaries:

$$NO_{i,N_{\mathrm{grid}}} = NO_{i,N_{\mathrm{grid}}-2} \tag{18}$$

$$NO_{N_{\mathrm{grid}},i} = NO_{N_{\mathrm{grid}}-2,i} \tag{19}$$

$$NO_{i,-1} = NO_{i,1} \tag{20}$$

$$NO_{-1,i} = NO_{1,i} \tag{21}$$

3.) Dirichlet boundary conditions with $NO = NO_{\text{bound.}}$ at the boundaries. 163

Neumann boundary conditions were used for most of the simulations if not explicitly 164
stated otherwise. This decision relates to the previously described mechanism of 165
synaptic growth: Neurons placed close to the edge of the sheet have a lower connection 166
probability due to the absence of neighboring neurons in the direction perpendicular to 167
the close-by border. It therefore models the synaptic growth within a square "cutout" 168
of neural tissue. The Neumann boundary condition fits into this picture since it allows a 169
zero-flux condition at the borders. This is a reasonable assumption, because NO 170
molecules cannot diffuse out of the tissue (unless they were placed in a surrounding 171
fluid). 172

Eq. (11) describes the influx of [NO] as a sum of scaled and spatially shifted Dirac 173
functions. Apart from the question whether this source term results in a well defined, 174
finite analytic solution at the neurons' positions (see Section *Spatial configuration of* 175
neurons allows for the precise prediction of firing rates), it can only be modeled to a 176
certain degree of accuracy depending on the resolution of the numeric grid. In practice, 177
we approximated the point sources of NO as insertions at individual grid cells at a rate 178
of $[\text{nNOS}]_i(t)/h^2$, where the normalizing divisor h^2 ensured the desired total influx per 179
neuron. This numeric implementation required two additional constraints: First, all 180
random neuron positions were confined to integer multiples of h in x- and y-direction. 181
Second, to avoid redundancy and for physiological reasons, each grid cell could only 182
hold one neuron at maximum. 183

Software 184

The Neural Network was simulated in python using the BRIAN spiking neural network 185
simulator package [24]. Plots were generated using the Matplotlib python package [25]. 186
Fitting of the power-law exponent of synaptic lifetimes was done with the *powerlaw* 187
python package [26], which used a maximum-likelihood method to fit power-law 188
exponents to the lifetime data. 189

Results 190

Distribution of firing rates 191

Fig. 1A–D shows a first result for the distribution of firing rates, comparing both 192
homeostatic mechanisms. As expected, non-diffusive homeostasis led to a sharp 193
distribution of firing rates at 3 Hz. Diffusive homeostasis indeed resulted in a much 194
broader distribution of mean firing rates. In panel A, we found a skewness of 195
$v_{\text{diff.}} = 0.765$ for diffusive homeostasis. To assess whether the statistics resemble a 196
log-normal distribution, we also plotted the distribution of decadic logarithms of firing 197
rates in Fig. 1B and D. Panel B shows the distribution of the decadic logarithms of 198
excitatory firing rates, being well fitted by a normal distribution. Inhibitory firing rates 199
were relatively unaffected by changing the homeostatic mechanism, see panels C and D. 200

Sweeney et al. found that diffusive homeostasis maintains the broadness of the 201
distribution of firing rates across a wide range of diffusion constants but rapidly 202
approaching zero for small values (cf. [13], Fig. 3C). We were able to reproduce this 203
result, see Fig. 1E. Homeostasis reaches a point of saturation, where faster diffusion has 204
no effect on the heterogeneity of firing rates. Each of the data points in Fig. 1E and F 205
corresponds to a single full simulation, though the same simulation data was used in A 206
and B. 55 simulations were run in total. We picked the D-values by hand to achieve a 207
good representation of the overall trend while limiting the amount of simulations. The 208
set of diffusion constants used is given in Table 4. We also investigated the influence of 209
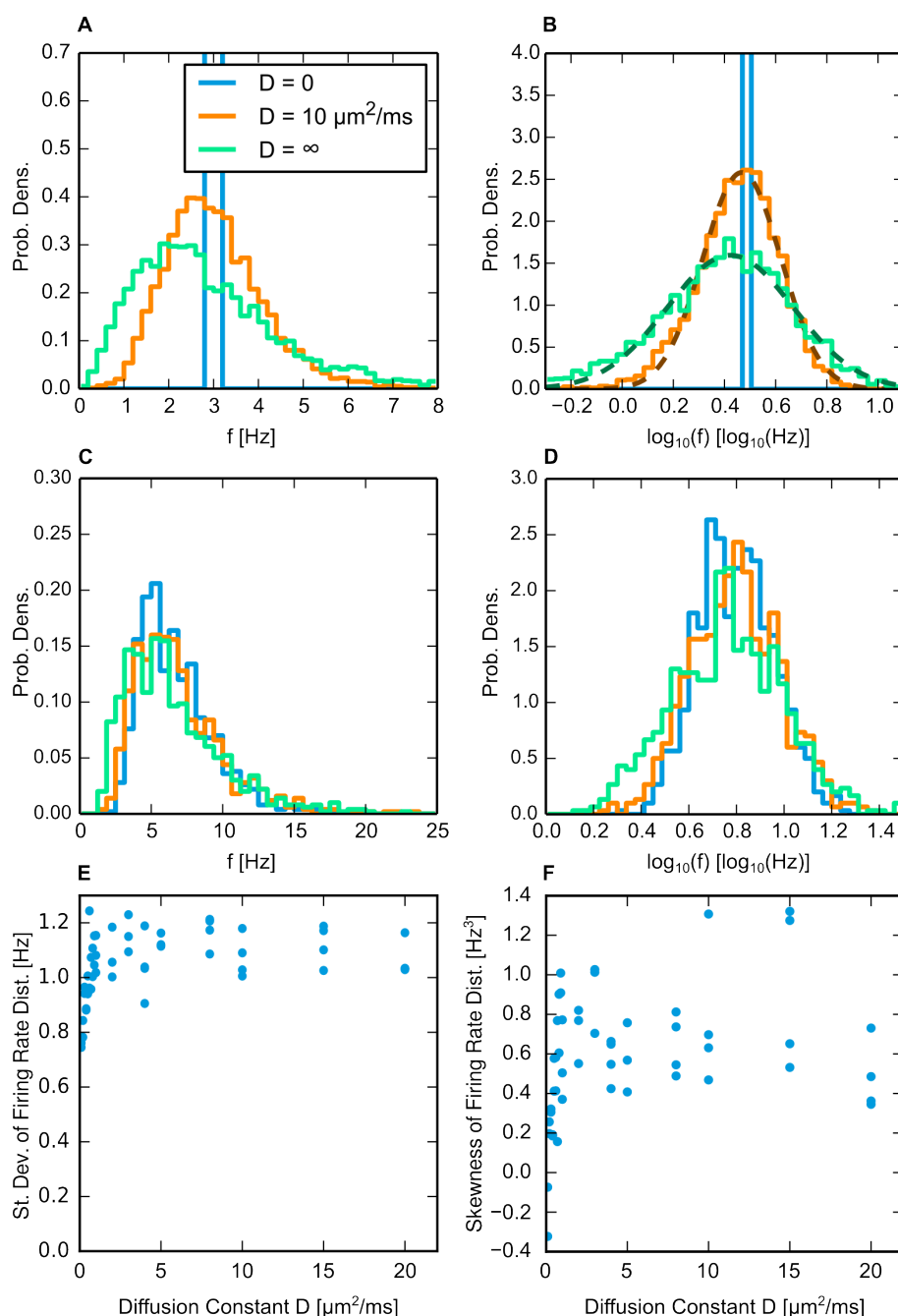
Fig 1. Distribution of firing rates. A,B,C,D: Histograms of mean firing rates over the excitatory (A/B) and inhibitory (C/D) population in regular (A/C) and logarithmic space (B/D). Distributions were generated from 10 simulation runs, 1 simulation was used for non-diffusive homeostasis. Mean firing rates were calculated from spikes within $1000\,\mathrm{s} \leq t \leq 1500\,\mathrm{s}$. **E,F**: Standard deviation (E) and skewness (F) of firing rate distribution of excitatory neurons (Neumann boundary conditions). Each data point was generated from one full simulation.

Table 4. Diffusion constants and number of simulations used in Fig. 1E and F.

D [$\mu m^2 ms^{-1}$]	Number of Sim.
0.0	1
$0.1, 0.2, ..., 0.8, 0.9$	2
$1.0, 2.0, ..., 5.0, 8.0, 10.0, 15.0, 20.0$	4

the diffusion constant onto the distribution's skewness, shown in Fig. 1F, to further quantify this dependence. Compared to the standard deviation, we saw a similar but not as clear trend with a drop for very small diffusion constants, even occasionally resulting in a left-skewed distribution (negative D-values).

A naturally emerging question when altering the diffusion constant is how excitatory firing rates behave in the absolute limit of infinitely fast diffusion. In fact, this case is quite easy to implement in the simulation: One simply has to feed all NO sources into a single scalar variable of NO concentration. This then provided the same NO readout for all excitatory neurons, which means that all excitatory thresholds changed at the same rate all the time, only shifting their initial distribution. Therefore, the effect of this particalur distribution will remain present for the entire simulation, and a larger variance among excitatory thresholds will likely also broaden the distribution of firing rates. However, we chose to set all excitatory thresholds to the same initial value. Fig. 1A–D shows the distributions for this case. As one can see, this results in a similar but broader log-normal like distribution of excitatory firing rates, going along with a more pronounced skewness of 1.51.

Non-random features of network topology and dynamics are preserved

While we explicitly intended altering the statistics of excitatory firing rates by implementing diffusive homeostasis, we wanted to preserve what has previously been reported by Miner and Triesch regarding the evolution and structure of recurrent excitatory weights [27]. More specifically, we were concerned with the following features of synaptic topology and dynamics: First, an overrepresentation of excitatory bidirectional connectivities, a feature found to be present in cortical networks [3]. Second, a power-law distribution of synaptic lifetimes. Loewenstein et al. reported on this feature in a study on the auditory cortex of mice [28]. Third, a heavy-tailed, log-normal distribution of synaptic efficacies, which have been observed in a number of experimental studies [3, 4, 29, 30].

Fig. 2 summarizes the results regarding these properties. As shown in Fig. 2A and B, Diffusive homeostasis leads to the same stable level of recurrent excitatory connection fraction, as well as an over-representation of bidirectional connections.

Fig. 2C shows that a log-normal like distribution of excitatory weights is preserved under diffusive homeostasis. Theoretical approaches to explaining this propoerty are mainly based on a combination of multiplicative and additive weight dynamics [61, 62], which is in line with our implementation of multiplicative normalization and additive STDP.

Fig. 2D illustrates the preservation of a power-law distribution of recurrent excitatory synaptic lifetimes during the steady phase of connectivity. Given the assertion that the slope of this distribution is linked to the overall balance of synaptic potentiation and depression [27], we can assume that both types of homeostasis result in a similar net difference between potentiation and depression.
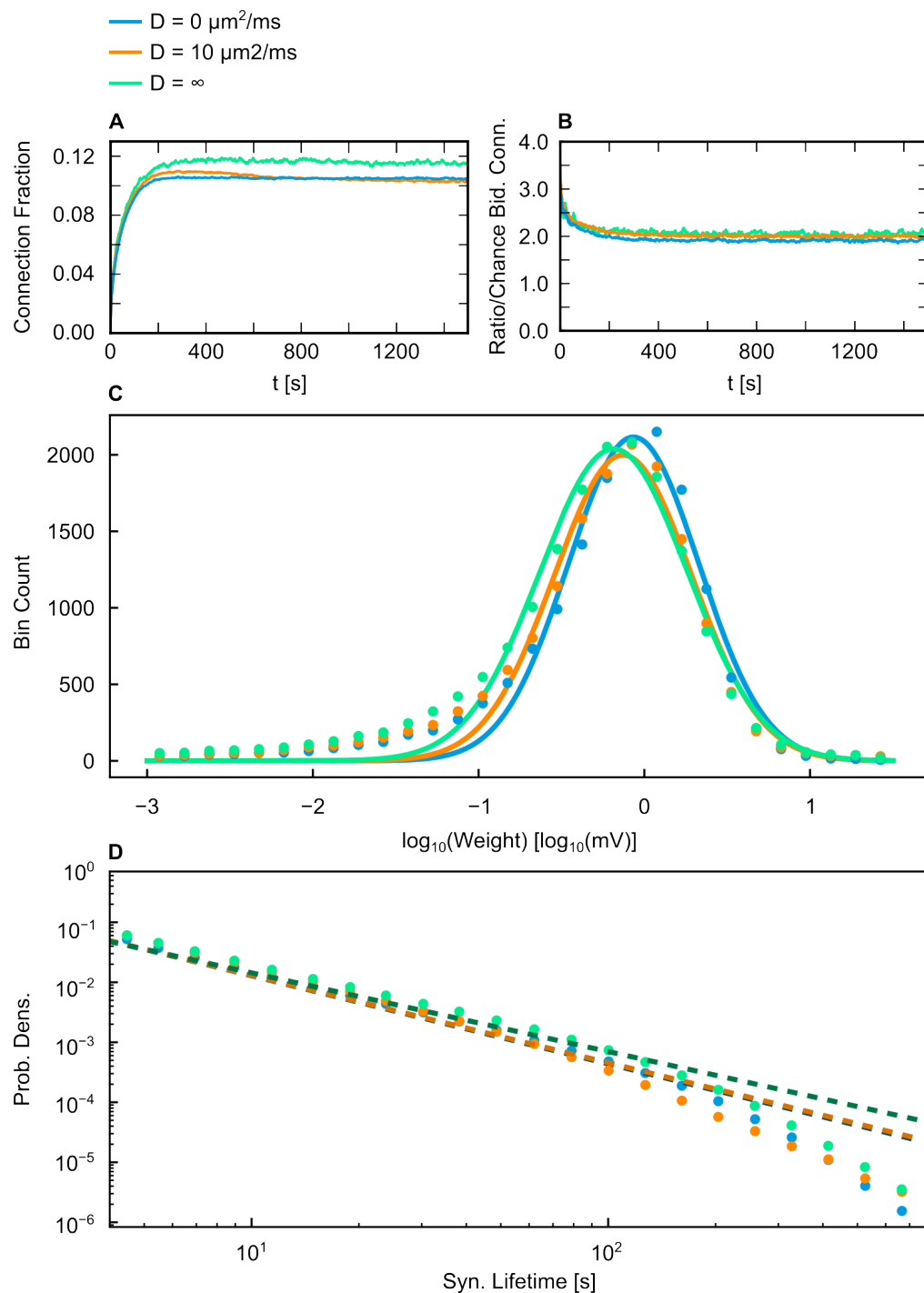
Fig 2. Time course of recurrent excitatory connection fraction. A: Evolution of recurrent excitatory connection fraction. **B**: Ratio of bidirectional connections relative to a random Erdős-Renyi graph. **C**: Distribution of excitatory recurrent weights after 1500 s. Solid curves are Gaussian fits. Data for each diffusion constant was taken from 5 simulations. **D**: Distribution of recurrent excitatory synaptic lifetimes. Single-trial data. Solid lines are estimates of a power-law exponent, giving a slope of approximately −1.9 for diffusive homeostasis and −1.7 for non-diffusive homeostasis. 5 simulation runs were used for each curve in panels A and B, panels C and D show representative single-trial data.

Heterogeneity of firing rate leads to the emergence of strongly influential excitatory neurons

Having established that the model accounts for above-chance bidirectional connectivities, a log-normal distribution of recurrent excitatory weights and a power-law distribution of synaptic lifetimes in the same way as its predecessor, we sought for possible differences within our network topology as a result of diffusive homeostasis. Since we only implemented synaptic normalization for the sum of ingoing weights, the total or average strength of *outgoing* connections may vary from cell to cell. In a sense, the strength of outgoing connections per neuron can be regarded as a measure of how influential a neuron's activity is with respect to other neurons in the network. Effenberger et al. have proposed a model where such "driver neurons" form highly active and interconnected subnetworks [31], an observation that is backed up by experimental studies [32, 33]. Fig. 3A shows that diffusive homeostasis allows for the emergence of a small group of highly influential neurons, which resembles the findings in [31]. A comparison of statistics generated with shuffled versions of the weight matrices illustrates that above-chance exceptionally strong mean outgoing weights were indeed present. Statistical significance of the differences depicted in Fig. 3A was additionally tested by means of a two-sample Kolmogorov-Smirnov test ($p < 10^{-30}$).

Synapses between highly active presynaptic cells and postsynaptic neurons with lower activity are known to be subject to long-term potentiation [34, 35]. With this causal relation in mind, we can argue that diffusive homeostasis effectively embodies a similar functional role as inhibitory STDP in [31] by allowing for the presence of excitatory cells with above-average activity. We tested this relationship by plotting the mean outgoing weights against the average firing rate, see Fig. 3B. A strong heterogeneity of firing rates allowed for the development of few neurons with comparably strong mean outgoing weights, while the distribution of mean weights resulting from a narrow distribution is limited to a smaller range. We also tested the case of instantaneous diffusion. Mean weights did not reach as high values as in the case of diffusion at a finite rate.

Experimental studies have not only considered the presence of neurons with strong influence onto other neurons [33], but also found evidence that highly active neurons form subnetworks with an increased connectivity, in the sense that these cells are more likely than average to connect to each other, see [32]. We tested this in our network by evaluating the connection fraction among the top 10% of excitatory neurons with respect to their average firing rate within $1000\,\text{s} \leq t \leq 1500\,\text{s}$ and comparing it to the rest of the excitatory population and the same calculation for the non-diffusive case. This returned CF = 0.1371 ± 0.0061 for the top 10% and CF = 0.0982 ± 0.0013 for the lower 90% in the case of diffusive homeostasis, and CF = 0.0954 ± 0.0044 for the top 10% and CF = 0.0992 ± 0.0002 for the lower 90% in the case of non-diffusive homeostasis. Standard errors were calculated from 5 simulation runs for each homeostatic mechanism, and connectivity matrices were taken from t = 1500 s. This showed that connectivity is indeed increased among the fastest-firing 10% of the neurons in the case of diffusive homeostasis. Effenberger et al. reported a similar effect, in fact with even more pronounced differences of connectivity [31].

Spatial configuration of neurons allows for the precise prediction of firing rates

Having analyzed the distribution of firing rates resulting from the implementation of diffusive homeostasis, we were interested in how strongly the actual positioning of excitatory neurons influences the resulting statistics of firing activity. To do so, we assumed that the spontaneous firing measured during the stable phase of the network,
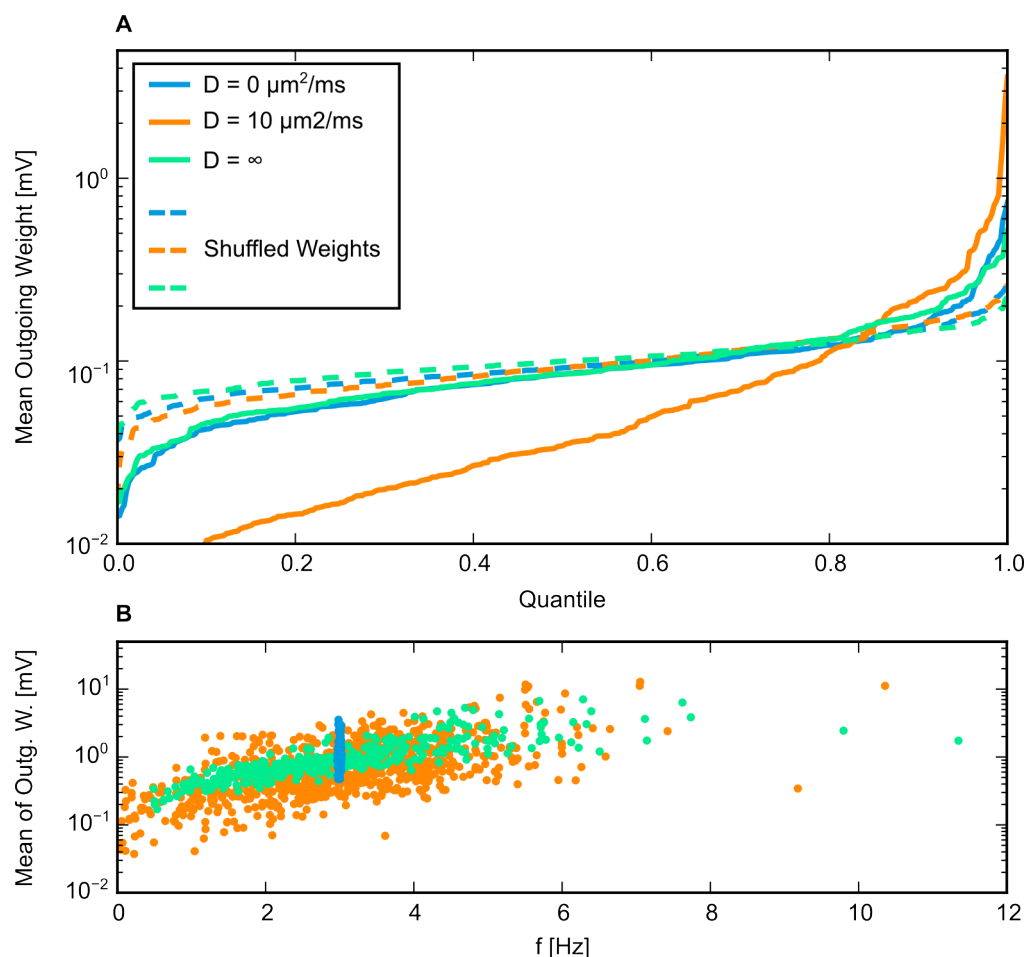
Fig 3. Quantile function of mean excitatory outgoing weights. A: Mean of outgoing weights of excitatory neurons in order sorted by magnitude. Dashed lines are means obtained by randomly shuffling synaptic weights. Single trial data. **B**: Mean of outgoing excitatory weights at $t = 1500\,s$ plotted against mean presynaptic firing rate (averaged over $700\,s \leq t \leq 1000\,s$) in logarithmic space. Each point corresponds to a presynaptic excitatory cell. Two simulation runs were used for diffusive homeostasis, all other are single-trial data.

characterized by a constant excitatory connectivity, can be regarded as a homeostatic steady state. Given no sudden strong changes of neural input, the homeostatic feedback levels out the error signal, given by $[NO] - [NO]_0$ to approximately zero, since Eq. 12 is a realization of an integral control. Our search for the steady-state configuration of firing rates thus reduced to finding a set of firing rates that led to a concentration level of $[NO]_0$ at every excitatory neuron's position:

$$[NO](\mathbf{x}_{\text{neur.},i}) = [NO]_0 \,,\, \forall i \,. \tag{22}$$

Furthermore, we found that the nonlinearity between spiking activity and NO synthesis could be well approximated by a linear relation between average firing rate r_i and rate of NO synthesis $nNOS_i$ by

$$[\text{nNOS}]_i = \frac{Ca^{2+}_{\text{spike}}^3 \tau_{\text{Ca}^{2+}} \ln(2)}{3} \cdot r_i \equiv \gamma r_i \,. \tag{23}$$

See Appendix S1 for a derivation of the proportionality factor. Given this simplification, the steady state of NO concentration is thus defined by the solution of

$$0 = -\lambda[NO] + D\nabla^2[NO] + \sum_i \delta^2(\mathbf{x} - \mathbf{x}_{\text{neur.},i}) \cdot \gamma \cdot r_i \tag{24}$$

which can be reformulated to

$$\left(\nabla^2 + \left(i\sqrt{\frac{\lambda}{D}}\right)^2\right)[NO] = \sum_i \delta^2(\mathbf{x} - \mathbf{x}_{\text{neur.},i}) \cdot \frac{-\gamma \cdot r_i}{D} \tag{25}$$

which is a two-dimensional Helmholtz equation. Its Green's function is

$$[NO](\mathbf{x}) = \frac{r_i \gamma}{2\pi D} K_0\left(|\mathbf{x}|\sqrt{\frac{\lambda}{D}}\right) \equiv r_i \cdot \psi_{\text{point}}(|\mathbf{x}|) \tag{26}$$

where K_0 is the zeroth modified Bessel function of the second kind [36]. This solution reveals a fundamental problem of modeling the sources of NO production as point sources: the fact that $K_0(x)$ diverges to infinity for $x \to 0$. It is merely due to the finite density of the numeric grid used for the simulation of diffusion that allows for a finite target value of concentration.

Generally speaking, no matter how the actual shape of the numeric solution in the equilibrium at a constant production rate looks like, it must be of the form

$$[NO]_i(\mathbf{x}) = r_i \cdot \psi(|\mathbf{x}_{\text{neur.},i} - \mathbf{x}|) \,. \tag{27}$$

The full solution is then

$$[NO](\mathbf{x}) = \sum_i [NO]_i(\mathbf{x}) \,. \tag{28}$$

By defining

$$\psi_{ij} \equiv \psi_{ij} \equiv \psi(|\mathbf{x}_{\text{neur.},i} - \mathbf{x}_{\text{neur.},j}|) \tag{29}$$

we could express condition (22) as

$$\sum_j \psi_{ij} \cdot r_j = [NO]_0 \tag{30}$$

or, as an operator

$$\hat{\psi}\mathbf{r} = [NO]_0 \mathbf{n} \tag{31}$$

$$\mathbf{n} \equiv (1, 1, ..., 1) \,. \tag{32}$$

The problem of finding the steady-state solution of the homeostatic constraint thus reduced to inverting $\hat{\psi}$:

$$\mathbf{r} = [\text{NO}]_0 \hat{\psi}^{-1} \mathbf{n} \tag{33}$$

Still, we had to find a modified, non-diverging version of $\psi(\text{d}(\mathbf{x}_{\text{neur.,i}}, \mathbf{x}))$ to acquire any prediction from this model. It had to retain the shape given by (26) for larger distances but approach the correct numeric error value at the origin, determined by the spacing of the numeric grid. We solved this problem by the following expression:

$$\psi_{\text{approx.}} \equiv \frac{1}{\left(\frac{1}{\psi_0^{\varepsilon}} + \frac{1}{\psi_{\text{point}}^{\varepsilon}} \right)^{\frac{1}{\varepsilon}}} \tag{34}$$

where ε determines the "smoothness" of transition between ψ and the cutoff value ψ_0. We chose $\varepsilon = 10$ for all further calculations. We took the simple approach of interpreting this value as a mean of the analytic solution across the area covered by the corresponding grid cell to find an expression for ψ_0. As an additional simplification, we substituted the necessary integration over the square grid cell by a circular area of equal size around the source. This calculation yielded

$$\psi_0 = \gamma \frac{1 - h\sqrt{\frac{\lambda}{\pi D}} K_1 \left(h\sqrt{\frac{\lambda}{\pi D}} \right)}{h^2 \lambda} \tag{35}$$

where h is the spatial resolution of the grid cells.

By simply calculating all matrix elements of $\hat{\psi}$ by means of Eq. (29), one would neglect the finite boundaries of the system, which would cause neurons close to the edge to "bleed" into empty space. We accommodated for zero-flux Neumann boundary conditions by adding appropriately mirrored copies of the neurons' positions, canceling the orthogonal component of the gradient at the boundaries.

After having worked out the analytical basis, we compared the prediction obtained from numerically solving Eq. (31) for certain spatial configurations of neurons to the steady-state firing rates of the full spiking network with the same spatial structure. As Fig. 4A shows, the actual shape of the distribution was well predicted by the solution of the linear system. Furthermore, we were particularly interested in the quality of the predictions with respect to the choice of diffusion constant. Fig. 4B shows three examples: For $D = 10\,\mu\text{m}^2\text{ms}^{-1}$, the correlation between measured and predicted firing rates is very good. In contrast, we included the - obviously unsuccessful - attempt to predict firing rates for a simulation with instantaneous diffusion based on the spatial structure by setting D to a relatively high value of $D = 100\,\mu\text{m}^2\text{ms}^{-1}$. This represented a limiting case where our analytic model could not make any meaningful predictions, since instantaneous diffusion overrides any spatial inhomogeneities. The outcome of the third case shown in the plot, $D = 0$, is correctly predicted by the analytic model. In general, instantaneous diffusion as well as $D = 0$ overrode the effects of spatial heterogeneity onto firing rates.

These observations naturally led us to the question of how the correlation between predicted and measured firing rates behaves in between the aforementioned limits. Especially, we were interested in the range of the diffusion constant for which our model provides a good description of the full spiking network's activity. Fig. 4C depicts the Pearson correlation coefficient of $f_{\text{matrix,predict.}}$ and $f_{\text{sim.}}$ against the diffusion constant used in the simulation. A relatively high correlation was obtained for a wide range of diffusion constants. However, we could see a general decline of correlation for larger diffusion constants. This trend was in line with the aforementioned limit of instantaneous diffusion, namely a complete decorrelation between prediction and measurement, as well as the good agreement for $D = 10\,\mu\text{m}^2\text{ms}^{-1}$ shown in Fig. 4A.
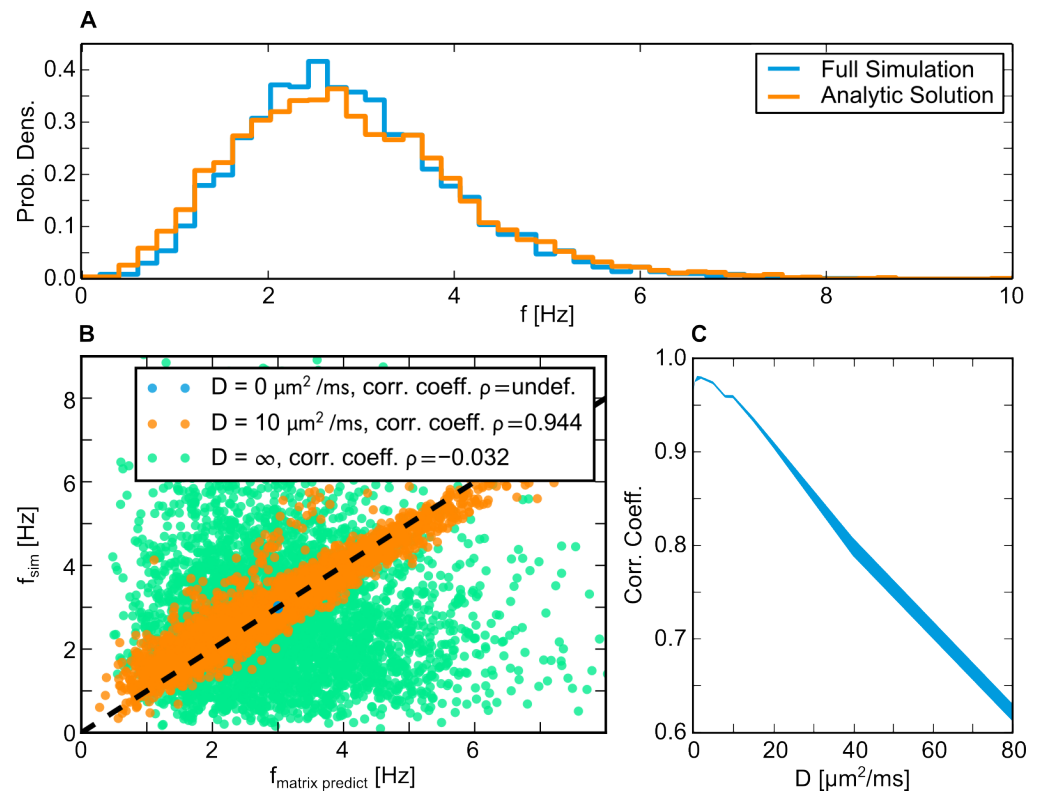
Fig 4. Empirical distribution of excitatory firing rates and theoretical prediction. **A**: Distribution of firing rates for $D = 10\,\mu m^2 ms^{-1}$, full simulation and analytic prediction. Data was taken from 10 simulation runs. **B**: Measured firing rates ($1000\,s \leq t \leq 1500\,s$) versus predicted firing rates based on the solution of Eq. (31). For $D = \infty$ (instantaneous diffusion in the full simulation), the analytic prediction was calculated with a comparably large diffusion constant of $D = 100\,\mu m^2 ms^{-1}$. Plot shows representative single-trial data. **C**: Pearson correlation coefficient of predicted and measured firing rates (see Panel C) versus diffusion constant. Line width depicts standard error, 5 simulations were used for each D-value.

Having acknowledged the good agreement between the full network simulation and the predictions of our simplified model, we also made predictions for more realistic settings of spatial densities. Although neuronal densities can vary considerably across different cortical areas and species [37], we considered a density of $9 \cdot 10^4 \, \text{mm}^{-3}$ as a realistic value [38]. This corresponds to a mean free path of $22.31 \mu \text{m}$. On a single two-dimensional slice of $1000 \times 1000 \, \mu\text{m}$, one should therefore populate approximately 2000 neurons to achieve the same mean free path. For the sake of a larger sample set, we calculated the homeostatic equilibrium for 8000 randomly placed cells on a $2000 \times 2000 \, \mu\text{m}$ sheet. As shown in Fig. 5 (blue histogram), this resulted in an equally shaped, skewed distribution of firing rates.

Two other variants of diffusion and cell placement are also shown in Fig. 5: $9 \cdot 10^4$ randomly placed cells in a cube of $1 \, \text{mm}^3$, and a single, flat layer of 8000 cells (random x- and y-position, fixed z-coordinate) in a $2000 \times 2000 \times 1000 \, \mu\text{m}$ cuboid. While the former case mimics a uniform neuronal structure, the latter was meant to mimic interaction solely across a single cortical layer. All other diffusion parameters (λ and D) were kept at their standard values. The resulting firing rate distributions are depicted in Fig. 5. Both variants in 3D space yielded similar distributions, which, however, differed from the original setup with respect to variance and skewness, both being reduced.

Given the good predictions of firing rates of our simplified mathematical model under the standard configuration, these additional predictions suggest the implementation of a full network simulation combined with 3D diffusion for further testing of the homeostatic model. Apparently, the fact that diffusion in three dimensions results in a more localized fundamental solution of a single point source compared to two dimensions leads to a reduced intercellular overlay of homeostatic signals. We also noticed that the width of the distributions could not be further broadened artificially by increasing the the diffusion constant to very high values.

Low-density neighborhoods correlate with strong outgoing connections

We previously stated that diffusive homeostasis allowed the network to develop few neurons with exceptionally strong outgoing weights. We found this effect to be present in neurons with an highly above-average firing rate. Moreover, our analytical predictions of individual neuronal activity suggest that the steady state of firing rates is strongly influenced by the spatial structure of excitatory neurons. Combining these two qualities led us to the conclusion that one should be able to observe some relation between spatial structure and the emergence of "driver neurons". More specifically, regions of neurons with above average firing rates should develop stronger outgoing connections. We approximated the local neuron density by means of a a Gaussian kernel with $\sigma = 50 \, \mu\text{m}$ to test this hypothesis. Fig. 6 shows the results. Despite a certain amount of randomness, our prediction was indeed verified.

Discussion

The LIF-SORN in combination with diffusive homeostasis presents oneself as the first *self-organizing* model of cortical activity and plasticity to exhibit core features of neuronal firing statistics as well as synaptic connectivity and dynamics. In order to acquire a deeper understanding of the mechanisms that determine neuronal activity we developed an analytical expression that allowed us to reliably predict the steady-state of firing rates based on the spatial structure of excitatory neurons. We would like to emphasize that this explanation differs from common approaches of understanding the emergence of heavy-tailed statistics of firing rates in recurrent networks. Theoretical
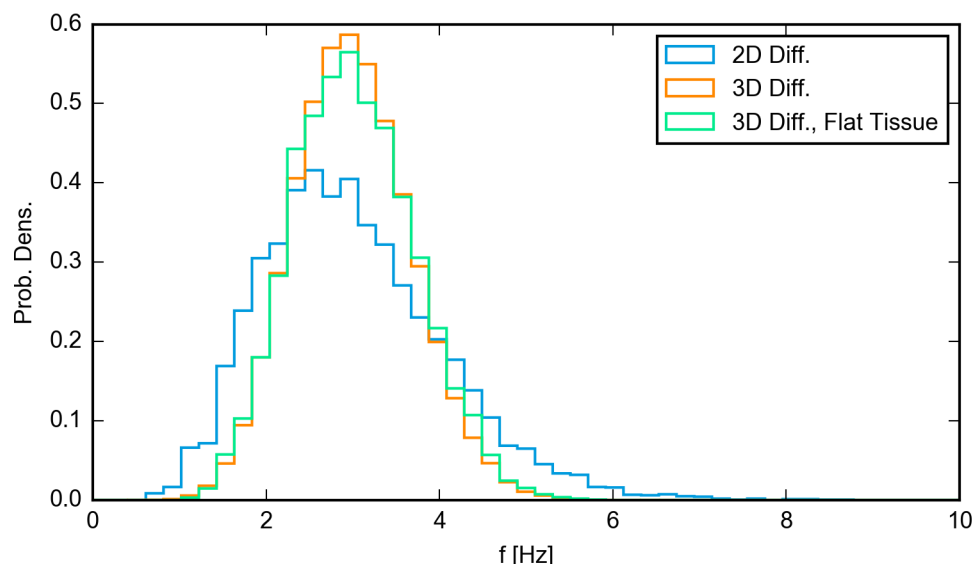
Fig 5. Distribution of firing rates acquired by solving the diffusive homeostatic fixed point. 2D variant was carried out on a $2000 \times 2000\,\mu\text{m}$ sheet (grid resolution 200×200) and 8000 randomly picked cell positions. 3D variant used a $1000 \times 1000 \times 1000\,\mu\text{m}$ cube (grid resolution $100 \times 100 \times 100$) and $9 \cdot 10^4$ random cell positions. 3D variant with a flat neural tissue used a $2000 \times 2000 \times 1000\,\mu\text{m}$ cube (grid resolution $200 \times 200 \times 100$) and 8000 cell positions with random x- and y-coordinates and a z-coordinate fixed at $500\,\mu\text{m}$. All graphs depict single-trial data.

studies on the behavior of recurrent networks are largely based on the assumption that the excitability of neurons is not individually fine-tuned but rather randomly distributed and adjusted globally to achieve a desired mean firing rate. Predictions about the resulting activity are then made based on (potentially simplified) statistical features of recurrent connectivity and/or the specific form of the neuronal transfer function used in the model, see e.g. [10, 11, 39]. Our interpretation of our results led us to the conclusion that this approach matches the limiting case of instantaneous diffusion: While Fig. 1A–D did not reveal many differences between finite-velocity and instantaneous diffusion in terms of overall statistics, the decorrelation shown in Fig. 4C suggests that increasing the diffusion constant goes along with a transition between a spatially determined configuration of excitatory firing rates and a network topology-determined behavior.

By analyzing network activity based on our analytic model, we found that indeed only a single homeostatic fixed point exists for finite diffusion constants. On a practical level though, the gradual decorrelation with this theoretical state of activity upon larger values of D was presumably caused by synaptic turnover which changed the synaptic input, since fluctuations of synaptic input were more slowly and less accurately compensated in the case of larger diffusion constants. However, for the standard choice of parameters (being roughly based on experimental data) the resulting activity was indeed strongly bound to the spatial structure of excitatory cells. Naturally, this raised the question of biological plausibility. To our knowledge, no experimental study exists that relates measurements of spontaneous activity to local fluctuations of neuronal densities. Interestingly, measurements in the barrel cortex and hippocampus have found that firing rates during exploration or task performance are significantly correlated with those found for spontaneous, baseline activity [2, 40]. This suggests that the same set of neurons tend to be relatively active or inactive under different stimuli and changing
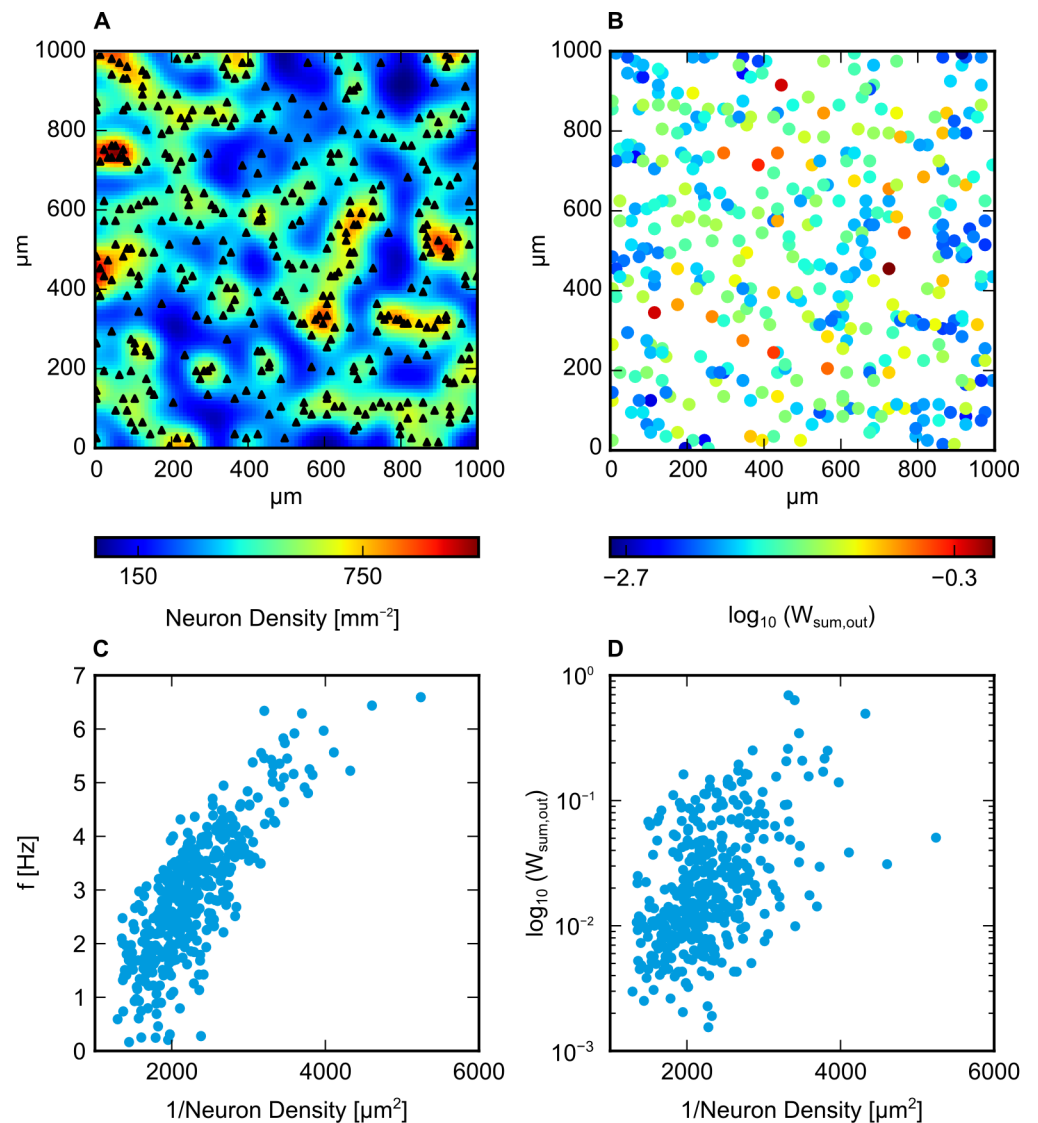
Fig 6. Mean outgoing excitatory weights vs. reciprocal neuron density. A: Scatter-plot of excitatory neurons' positions and local neuron density (calculated by convolution with a Gaussian kernel with $\sigma = 50\,\mu\mathrm{m}$). **B**: Decadic logarithm of outgoing excitatory weights. Note the spatial correlation between **A** and **B** in high/low-density regions. **C**: Frequency of excitatory weights (averaged over $1000\,\mathrm{s} \leq t \leq 1500\,\mathrm{s}$) versus reciprocal neuronal density (same estimation method as in A). Coefficient of correlation $\rho = 0.798$. **D**: Decadic logarithm of mean outgoing excitatory weights versus reciprocal neuronal density. Coefficient of correlation $\rho = 0.513$.

environments. In the light of these observations, one might speculate whether random spatial positioning might at least partially act as a determinant of these individual homeostatic working points of firing activity. A possible reason for the strong influence of spatial structure in the implemented model could be the fact that cells were modeled as approximate point sources. This allowed for a clear distinction between individual cells, even in close vicinity. While Sweeney et al. argued that the size of the studied tissue is large compared to the size of individual somata (which, apparently, they claim to be the main source of nitric oxide), Philippides et al. reported that NO is often synthesized in a more delocalized way by means of fine fibers originating from the soma [41]. The diameter of these "production areas" is on the order of $10 - 100\mu m$. This might explain why in reality diffusive homeostasis may not act as much as a precise tuner of single neuron activities as found in the computational model. We have shown that the predictions of our analytic approach to obtaining neuronal firing rates are consistent when using more realistic two-dimensional neuronal densities. Interestingly, the predictions for three-dimensional spatial interaction were less encouraging in terms of broadness and skewness of the resulting firing rate distribution. Still, since some amount of heterogeneity could still be observed, we consider it possible that local bunching or isolation of neurons can induce a disposition towards lower/higher long-term firing rates.

The basic assumption that has to be made for this prediction to hold is that NO concentrations are tuned towards a target concentration across neuronal cell bodies. In the theoretical model we used, this was achieved by tuning neuronal excitability by means of a perfect integral control. This might be considered an oversimplification, but does reflect the general idea that NO concentrations must be held within some regime associated with normal neuronal activity. In consequence, it is reasonable to assume that the aforementioned implications of varying neuronal densities still hold at least qualitatively, even if the tuning of NO concentration is not as strict and exact as seen in the theoretical model.

Savin et al. showed that local lesions in a network subject to diffusive synaptic homeostasis can lead to significantly different, bursting network behavior [42]. This complements our results in the sense that it supports the general idea of diffusive processes affecting activity based on spatial inhomogeneities.

Despite these considerations regarding the effects of spatial structure onto individual firing rates, our modifications seem to be a plausible way of giving rise to many features of cortical structure and activity. Apart from the previously discussed properties of spiking activity, we have have shown that important features of synaptic topology and plasticity found in earlier research are compatible with diffusive homeostasis. We thereby created a model, which combines the here presented features of cortical structure with the desired statistics of neuronal activity. This was achieved without specific modifications of Hebbian plasticity rules, which have also been proposed as an explanation for log-normally distributed synaptic weights [9, 10, 31]. Sweeney et al. also included synaptic plasticity via STDP into their model, but did not include synaptic normalization, which led to a bimodal distribution of weights, instead of the log-normal shape we found [13].

In addition, we found that heterogeneity of firing rates led to a much more pronounced separation of mean outgoing weights in our network, which were positively correlated to presynaptic firing rates. This is in line with other theoretical and experimental observations, arguing that a small subset of highly active neurons may serve to form relatively strongly connected and stable subnetworks that can quickly react to momentary changes in the environment, while fine tuned adaptation involves the slower firing majority of cells [6, 32, 43].

As mentioned previously, the SORN has also proven its capabilities in associative

learning and inference tasks [44]. A logical step should thus be to test whether the new 492
features presented in this paper can enhance performance in learning, in the sense that 493
the computational and memory resources given by the network size are used more 494
efficiently. 495

Recent studies have brought up inhibitory-to-excitatory STDP with respect to 496
stabilizing network activity [45, 46]. Results similar to ours concerning network topology 497
have also been achieved with inhibitory STDP [31]. In terms of their functional role of 498
stabilizing network activity, it is reasonable to assume that both, diffusive homeostasis 499
and inhibitory STDP, can simultaneously act in a biological system. 500

References

1. Battaglia FP, Sutherland GR, Cowen SL, Mc Naughton BL, Harris KD. Firing rate modulation: A simple statistical view of memory trace reactivation. Neural Networks. 2005;18(9):1280 – 1291. doi:https://doi.org/10.1016/j.neunet.2005.08.011.

2. Mizuseki K, Buzsáki G. Preconfigured, skewed distribution of firing rates in the hippocampus and entorhinal cortex. Cell Reports. 2013;4.

3. Song S, Sjöström PJ, Reigl M, Nelson S, Chklovskii DB. Highly Nonrandom Features of Synaptic Connectivity in Local Cortical Circuits. PLOS Biology. 2005;3(3). doi:10.1371/journal.pbio.0030068.

4. Lefort S, Tomm C, Floyd Sarria JC, Petersen CCH. The Excitatory Neuronal Network of the C2 Barrel Column in Mouse Primary Somatosensory Cortex. Neuron. 2009;61(2):301–316. doi:10.1016/j.neuron.2008.12.020.

5. Buzsáki G, Geisler C, Henze DA, Wang XJ. Interneuron Diversity series: Circuit complexity and axon wiring economy of cortical interneurons. Trends in Neurosciences. 2004;27.

6. Buzsáki G, Mizuseki K. The log-dynamic brain: how skewed distributions affect network operations. Nature Reviews Neuroscience. 2014;.

7. Marsat G, Maler L. Neural Heterogeneity and Efficient Population Codes for Communication Signals. Journal of Neurophysiology. 2010;104(5):2543–2555. doi:10.1152/jn.00256.2010.

8. Statman A, Kaufman M, Minerbi A, Ziv NE, Brenner N. Synaptic Size Dynamics as an Effectively Stochastic Process. PLOS Computational Biology. 2014;10(10):1–17. doi:10.1371/journal.pcbi.1003846.

9. Gilson M, Fukai T. Stability versus Neuronal Specialization for STDP: Long-Tail Weight Distributions Solve the Dilemma. PLOS ONE. 2011;6(10):1–18. doi:10.1371/journal.pone.0025339.

10. Koulakov AA, Hromádka T, Zador AM. Correlated Connectivity and the Distribution of Firing Rates in the Neocortex. The Journal of Neuroscience. 2009;.

11. Roxin A, Brunel N, Hansel D, Mongillo G, van Vreeswijk C. On the Distribution of Firing Rates in Networks of Cortical Neurons. Journal of Neuroscience. 2011;31(45):16217–16226. doi:10.1523/JNEUROSCI.1677-11.2011.

12. Hengen KB, Torrado Pacheco A, McGregor JN, Van Hooser SD, Turrigiano GG. Neuronal Firing Rate Homeostasis Is Inhibited by Sleep and Promoted by Wake. Cell. 2016;165(1):180–191. doi:10.1016/j.cell.2016.01.046.

13. Sweeney Y, Kotaleski JH, Hennig MH. A Diffusive Homeostatic Signal Maintains Neural Heterogeneity and Responsiveness in Cortical Networks. PLoS Computational Biology. 2015;.

14. Zhang LI, Tao HW, Holt CE, Harris WA, Poo M. A critical window for cooperation and competition among developing retinotectal synapses. Nature. 1998;395:37–44.

15. Bi G, Poo M. Synaptic Modifications in Cultured Hippocampal Neurons: Dependence on Spike Timing, Synaptic Strength, and Postsynaptic Cell Type. The Journal of Neuroscience. 1998;18(24):10464–10472.

16. Froemke RC, Poo M, Dan Y. Spike-timing-dependent synaptic plasticity depends on dendritic location. Nature. 2005;434(7030):221–225.

17. Markram H, Wang Y, Tsodyks M. Differential signaling via the same axon of neocortical pyramidal neurons. Proceedings of the National Academy of Sciences. 1998;95(9):5323–5328.

18. Connors BW, Gutnick MJ. Intrinsic firing patterns of diverse neocortical neurons. Trends in Neurosciences. 1990;13(3):99 – 104. doi:http://dx.doi.org/10.1016/0166-2236(90)90185-D.

19. Benda J, Herz AVM. A Universal Model for Spike-Frequency Adaption. Neural Computation. 2003;15(11):2523–2564.

20. Desai NS, Rutherford LC, Turrigiano GG. Plasticity in the intrinsic Excitability of Cortical Pyramidal Neurons. Nature Neuroscience. 1999;2:515–520.

21. Dayan P, Abbott LF. Theoretical Neuroscience. MIT Press; 2001.

22. Hill A. The possible effects of the aggregation of the molecules of haemoglobin on its dissociation curves. The Journal of Physiology. 1910;40:iv—vii. doi:10.1113/jphysiol.1910.sp001389.

23. Philippides A, Husbands P, O'Shea M. Four-Dimensional Neuronal Signaling by Nitric Oxide: A Computational Analysis. Journal of Neuroscience. 2000;20(3):1199–1207.

24. Brette R, Goodman D, Stirnberg M. The Brian spiking neural network simulator (Version 1.0) [Computer Software]; 2016. `http://www.briansimulator.org/`. Available from: `http://www.briansimulator.org/`.

25. Team MD. Matplotlib (Version 1.5.3) [Computer Software]; 2016. `https://matplotlib.org/1.5.3/index.html`. Available from: `http://www.briansimulator.org/`.

26. Alstott J. powerlaw: A Python Package for Analysis of Heavy-Tailed Distributions (Version 1.4.1) [Computer Software]; 2017. `https://pypi.python.org/pypi/powerlaw`. Available from: `http://www.briansimulator.org/`.

27. Miner D, Triesch J. Plasticity-Driven Self-Organization under Topological Constraints Accounts for Non-Random Features of Cortical Synaptic Wiring. PLoS Computational Biology. 2016;.

28. Loewenstein Y, Yanover U, Rumpel S. Predicting the Dynamics of Network Connectivity in the Neocortex. Journal of Neuroscience. 2015;35(36):12535–12544. doi:10.1523/JNEUROSCI.2917-14.2015.

29. Yasumatsu N, Matsuzaki M, Miyazaki T, Noguchi J, Kasai H. Principles of Long-Term Dynamics of Dendritic Spines. Journal of Neuroscience. 2008;28(50):13592–13608. doi:10.1523/JNEUROSCI.0603-08.2008.

30. Loewenstein Y, Kuras A, Rumpel S. Multiplicative Dynamics Underlie the Emergence of the Log-Normal Distribution of Spine Sizes in the Neocortex In Vivo. Journal of Neuroscience. 2011;31(26):9481–9488. doi:10.1523/JNEUROSCI.6130-10.2011.

31. Effenberger F, Jost J. Self-Organization in Balanced State Networks by STDP and Homeostatic Plasticity. PLOS Computational Biology. 2015;.

32. Yassin L, Benedetti BL, Jouhanneau JS, Wen JA, Poulet JF, Barth AL. An Embedded Subnetwork of Highly Active Neurons in the Neocortex. Neuron. 2010;68(6):1043 – 1050. doi:http://dx.doi.org/10.1016/j.neuron.2010.11.029.

33. Eckmann JP, Jacobi S, Marom S, Moses E, Zbinden C. Leader neurons in population bursts of 2D living neural networks. New Journal of Physics. 2008;10. doi:10.1088/1367-2630/10/1/015011.

34. Sjöström PJ, Turrigiano GG. Rate, Timing, and Cooperativity Jointly Determine Cortical Synaptic Plasticity. Neuron. 2001;.

35. Feldman D. The Spike-Timing Dependence of Plasticity. Neuron. 2012;.

36. Couto RT. Green's functions for the wave, Helmholtz and Poisson equations in a two-dimensional boundless domain. Revista Brasileira de Ensino Física. 2013;.

37. Collins CE, Airey DC, Young NA, Leitch JH D B Kaas. Neuron densities vary across and within cortical areas in primates. Proceedings of the National Academy of Sciences of the United States of America. 2010;107.

38. Schüz A, Palm G. Density of neurons and synapses in the cerebral cortex of the mouse. The Journal of Comparative Neurology. 1989;286(4):442–455. doi:10.1002/cne.902860404.

39. van Vreeswijk C, Sompolinsky H. Chaotic Balanced State in a Model of Cortical Circuits. Neural Computation. 1998;.

40. O'Connor DH, Peron SP, Huber D, Svoboda K. Neural Activity in Barrel Cortex Underlying Vibrissa-Based Object Localization in Mice. Neuron. 2010;67.

41. Philippides A, Ott SR, Husbands P, Lovick TA, O'Shea M. Modeling Cooperative Volume Signaling in a Plexus of Nitric Oxide Synthase-Expressing Neurons. Journal of Neuroscience. 2005;25(28):6520–6532. doi:10.1523/JNEUROSCI.1264-05.2005.

42. Savin C, Triesch J, Meyer-Hermann M. Epileptogenesis due to glia-mediated synaptic scaling. Journal of the Royal Society Interface. 2008;.

43. Dragoi G, Harris KD, Buzsáki G. Place Representation within Hippocampal Networks Is Modified by Long-Term Potentiation. Neuron. 2003;39(5):843 – 853. doi:http://dx.doi.org/10.1016/S0896-6273(03)00465-3.

44. Hartmann C, Lazar A, Nessler B, Triesch J. Where's the Noise? Key Features of Spontaneous Activity and Neural Variability Arise through Learning in a Deterministic Network. PLOS Computational Biology. 2016;11(12):1–35. doi:10.1371/journal.pcbi.1004640.

45. Vogels TP, Sprekeler H, Zenke F, Clopath C, Gerstner W. Inhibitory Plasticity Balances Excitation and Inhibition in Sensory Pathways and Memory Networks. Science. 2011;334(6062):1569–1573. doi:10.1126/science.1211095.

46. Luz Y, Shamir M. Balancing Feed-Forward Excitation and Inhibition via Hebbian Inhibitory Synaptic Plasticity. PLOS Computational Biology. 2012;8(1):1–12. doi:10.1371/journal.pcbi.1002334.

Supporting information

S1 Appendix. We would like to derive a linear relation between mean firing rate and the mean rate of NO synthesis. One could naively replace the sum of Dirac functions in (9) by a continuous inflow $Ca_{\text{spike}}^{2+} r(t)$. This approximation would indeed allow for the correct calculation of a linear relation between mean firing rate and NO production if (10) was a linear homogeneous differential equation. The cubic dependence on Ca^{2+} breaks this simplicity. We note the following in order to derive an approximate description: The target firing rate of 3 Hz and the corresponding mean interspike interval of 0.33...s is large compared to the decay constant of calcium, $\tau_{\text{Ca}^{2+}} = 0.01\,\text{s}$. Consequently, it is very unlikely that one spike event will fall into a region where the calcium concentration, decaying from the instantaneous jump of the previous spike event, is still significantly larger than zero. In fact, calculating the mean concentration of Ca^{2+} before a new spike event over all neurons and all spike events for 1500 s resulted in a value of 0.0013. As such, one can justify the approximation of replacing the exact expression of $Ca^{2+3}(t)$, which is a cubed sum of cut off exponential functions, by a sum of cubed exponentials, because only one term of the sum at a time is significantly larger than zero:

$$
\begin{aligned}
Ca^{2+3}(t) &= \left[Ca_{\text{spike}}^{2+} \sum_i \theta\left(t - t_{\text{spike}}^i\right) \exp\left(-\left(t - t_{\text{spike}}^i\right)/\tau_{\text{Ca}^{2+}}\right) \right]^3 \\
&\approx Ca_{\text{spike}}^{2+\,3} \sum_i \theta\left(t - t_{\text{spike}}^i\right) \exp\left(-3\left(t - t_{\text{spike}}^i\right)/\tau_{\text{Ca}^{2+}}\right)
\end{aligned}
\tag{36}
$$

with $\theta(x)$ being the Heaviside step function. By the same argument

$$
\frac{Ca^{2+3}(t)}{Ca^{2+3}(t) + 1} \approx \sum_i \theta\left(t - t_{\text{spike}}^i\right) \frac{\exp\left(-3\left(t - t_{\text{spike}}^i\right)/\tau_{\text{Ca}^{2+}}\right)}{\exp\left(-3\left(t - t_{\text{spike}}^i\right)/\tau_{\text{Ca}^{2+}}\right) + \frac{1}{Ca_{\text{spike}}^{2+\,3}}} \ .
\tag{37}
$$

Therefore, the resulting rate of NO synthesis can be decomposed into a sum of time shifted responses onto a single kernel of calcium concentration as a result of a spike. For a spike at $t_{\text{spike}} = 0$, the solution of (10) can be calculated by

$$
\begin{aligned}
nNOS(t) &= \frac{1}{\tau_{\text{nNOS}}} \int_{-\infty}^{t} dt'\, \exp(-(t - t')/\tau_{\text{nNOS}})\theta(t') \frac{\exp(-3t'/\tau_{\text{Ca}^{2+}})}{\exp(-3t'/\tau_{\text{Ca}^{2+}}) + \frac{1}{Ca_{\text{spike}}^{2+\,3}}} \\
&= \frac{1}{\tau_{\text{nNOS}}} \int_{0}^{t} dt'\, \exp(-(t - t')/\tau_{\text{nNOS}}) \frac{\exp(-3t'/\tau_{\text{Ca}^{2+}})}{\exp(-3t'/\tau_{\text{Ca}^{2+}}) + \frac{1}{Ca_{\text{spike}}^{2+\,3}}} \ .
\end{aligned}
\tag{38}
$$

The exact solution of this integral can be expressed in terms of the hyper-geometric function, making it rather impractical for any further analysis. Looking for further simplifications, we noted that τ_{nNOS} is ten-fold larger than $\tau_{\text{Ca}^{2+}}$. This discrepancy in decay times allows for the assumption that the impact of the calcium kernel onto $nNOS$ is practically instantaneous. Consequently, $nNOS(t)$ becomes

$$
nNOS(t) = \frac{1}{\tau_{\text{nNOS}}} \theta(t) \exp(-t/\tau_{\text{nNOS}}) \int_{0}^{\infty} dt' \frac{\exp(-3t'/\tau_{\text{Ca}^{2+}})}{\exp(-3t'/\tau_{\text{Ca}^{2+}}) + \frac{1}{Ca_{\text{spike}}^{2+\,3}}} \ .
\tag{39}
$$

In this form, the integral has an easy-to-handle solution, which - with all spike events now included - results in

$$
nNOS(t) = \frac{Ca_{\text{spike}}^{2+\,3} \tau_{\text{Ca}^{2+}} \ln(2)}{3\tau_{\text{nNOS}}} \sum_i \theta(t - t_{\text{spike}}^i) \exp(-(t - t_{\text{spike}}^i)/\tau_{\text{nNOS}}) \ .
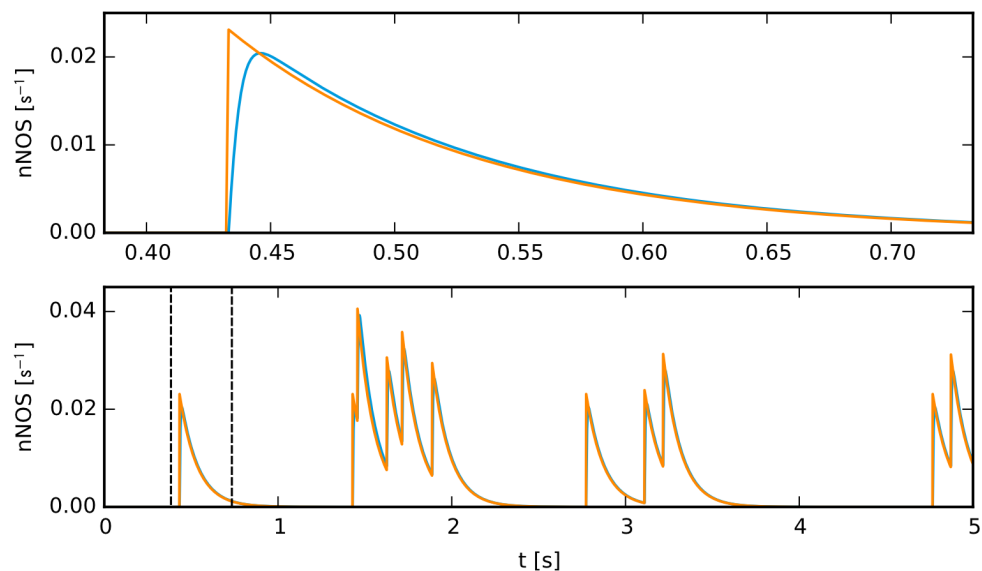\tag{40}
$$

Fig 7. nNOS under Poisson spiking. Time course of nNOS(t) with Poisson spiking at 3 Hz. The full simulation (blue, see equations (9),(10)) is well fitted by the simplified model (red, see Eq. (40)). Top axis is a closeup of the first spike event.

Fig. 7 compares the approximation given by (40) to the full NO production model (equations (9) and (10)). Spikes were drawn from a Poisson process at a rate of 3 Hz. The simplified model fits very well for sufficiently isolated spike events, as predicted. One can observe a slightly smaller but acceptable agreement for the rare event of two subsequent spikes appearing very close to each other, as seen in Fig. 7 at approximately 4 seconds.

Thus, on average, the sum in Eq. (40) simply reduces to the mean rate $\langle r \rangle$:

$$\langle nNOS \rangle = \frac{Ca_{\text{spike}}^{2+}{}^{3} \tau_{\text{Ca}^{2+}} \ln(2)}{3\tau_{\text{nNOS}}} \langle r \rangle \tag{41}$$